Inorganic Chemistry
Article
pubs.acs.org/IC

Magnetic and Neutron Diffraction Study on Melilite-Type Oxides $Sr_2MGe_2O_7$ (M = Mn, Co)

Takashi Endo,*[,†] Yoshihiro Doi,[†] Yukio Hinatsu,[†] and Kenji Ohoyama[‡]

[†]Division of Chemistry, Graduate School of Science, Hokkaido University, Sapporo 060-0810, Japan
[‡]Institute for Materials Research, Tohoku University, Sendai 980-8577, Japan

Ⓢ *Supporting Information*

ABSTRACT: The crystal structures and magnetic properties of melilite-type oxides $Sr_2MGe_2O_7$ (M = Mn, Co) were investigated. These compounds crystallize in the melilite structure with space group $P\overline{4}2_1m$, in which the M and Ge ions occupy two kinds of tetrahedral sites in an ordered manner. The magnetic M ions form a square-planar lattice in the *ab* plane. Both compounds do not show the structural phase transition down to 2.5 K. The temperature dependence of magnetic susceptibility for $Sr_2MnGe_2O_7$ shows a broad peak at ~6.0 K because of a two-dimensional magnetic interaction between Mn ions in the *ab* plane. At 4.4 K, an antiferromagnetic transition was observed. The magnetic structure was determined by the neutron powder diffraction measurements at 2.5 K. It can be represented by the propagation vector $k = (0, 0, 1/2)$, and the magnetic moments of Mn^{2+} (3.99 μ_B) ions order antiferromagnetically in a collinear manner along the *c* axis. On the other hand, $Sr_2CoGe_2O_7$ shows an antiferromagnetic transition at 6.5 K with divergence between zero-field-cooled and field-cooled susceptibilities. Its magnetic structure determined at 2.5 K has a magnetic propagation vector $k = (0, 0, 0)$, and the ordered magnetic moment of Co^{2+} (2.81 μ_B) adopts a collinear arrangement lying on the *ab* plane.

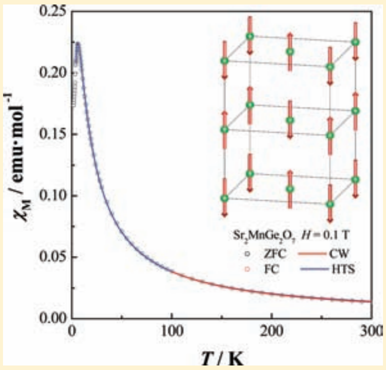

1. INTRODUCTION

Layered transition-metal oxides are potential targets for exploring interesting magnetic and electronic properties because of their low-dimensional characteristics.[1] As one of such fascinating systems, the magnetic properties of melilite-type oxides have been attracting interests. They have the general formula $A_2MM'_2O_7$ (A = larger cations, such as alkali earth and lanthanide ions; M, M′ = smaller divalent to tetravalent ions), and typically adopt a tetragonal structure (space group $P\overline{4}2_1m$) with a unit cell of $a \approx 8$ Å and $c \approx 5$ Å. The schematic crystal structure of the title compounds is illustrated in Figure 1. In this structure, the M and M′ ions occupy tetrahedral sites and these tetrahedra form a two-dimensional (2D) network in the *ab* plane, and larger A ions locate between the networks.[2−4]

The melilite-type oxides show a variety of magnetic properties,[5−16] as listed in Table 1. For example, $Ba_2MGe_2O_7$ (M = Mn, Co, Cu) show the 2D antiferromagnetic behavior due to the square-planar arrangement of the magnetic M ions, although the shortest M−M distance is along the *c* axis. At low temperatures, an antiferromagnetic transition (M = Mn),[9] a multiferroic behavior derived from antiferromagnetic and ferroelectric transitions under the magnetic field (Co),[10−14] and spiral antiferromagnetic ordering and incommensurate−commensurate magnetic transition (Cu) have been observed.[15] In addition, by introducing further magnetic ions into the M′ and A sites, the spin-glass behavior in $Ba_2Fe_2GeO_7$[17,18] and ferrimagnetic ordering between Eu^{2+} and Mn^{2+} moments in $Eu_2MnSi_2O_7$ have been found.[5]

To understand the structural and magnetic properties of melilite-type oxides, we focus our attention on the strontium melilites $Sr_2MGe_2O_7$ (M = Mn, Co). According to Naruse et al.,[19] these compounds are isostructural to the barium analogues; the substitution of Sr for Ba at the A site should shorten the M−M distance along the *c* axis. This may change the relationship between the intralayer and interlayer magnetic interactions in the melilites. Therefore, we investigated the syntheses, crystal structures, and magnetic properties of $Sr_2MGe_2O_7$ (M = Mn, Co, Zn) by means of X-ray and neutron powder diffraction, magnetic susceptibility, and specific heat measurements.

2. EXPERIMENTAL PROCEDURES

2.1. Synthesis. Polycrystalline samples (0.5 g) of $Sr_2MGe_2O_7$ (M = Mn, Co, Zn) were prepared by the standard solid-state reaction. As starting materials, SrO, $SrCO_3$, MnO, CoO, ZnO, and GeO_2 were used. The SrO was prepared by the decarbonation of $SrCO_3$ at 1400 °C for 12 h. These starting materials were weighed out in a stoichiometric ratio and well mixed in an agate mortar. The reaction mixture for $Sr_2CoGe_2O_7$ was calcined in air at 1200 °C for 12 h. For $Sr_2MnGe_2O_7$, the mixture was pressed into pellets and enclosed in a platinum tube. The platinum tube was then sealed in an evacuated quartz tube and heated at 1200 °C for 24 h.

2.2. Powder Diffraction Analysis. Powder X-ray diffraction (XRD) measurements were performed at room temperature using a Multi-Flex diffractometer (Rigaku) with a Cu K*α* X-ray radiation

Received: November 4, 2011
Published: February 29, 2012

dx.doi.org/10.1021/ic202386h | *Inorg. Chem.* 2012, 51, 3572−3578

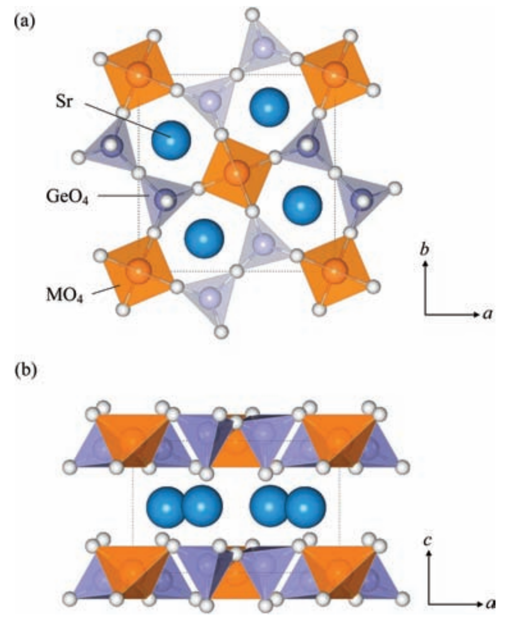

Figure 1. Schematic crystal structures of melilite-type oxides $Sr_2MGe_2O_7$ (M = Mn, Co): (a) viewed from the *c* axis, (b) projection of the structure in the *ab* plane.

Table 1. Magnetic Properties of Melilite-Type Oxides

sample	space group	T_c (K)	magnetic properties	ref
$Sr_2MnSi_2O_7$	$P\bar{4}2_1m$	3.4	antiferromagnet	5
$Ca_2CoSi_2O_7$	$P\bar{4}2_1m$	5.7	antiferromagnet	6
$Sr_2CoSi_2O_7$	$P\bar{4}2_1m$	≈7	antiferromagnet	6
$Ba_2CoSi_2O_7$	*C*2/*c*	≈5	antiferromagnet	6, 7
$BaCo_2SiO_7$	*C*2/*c*	21	antiferromagnet	7
$BaCu_2Si_2O_7$	*Pnma*	9.2	quasi-1D-AFM	8
$Sr_2MnGe_2O_7$	$P\bar{4}2_1m$	4.4	antiferromagnet, k = (0, 0, 1/2)	this study
$Sr_2CoGe_2O_7$	$P\bar{4}2_1m$	6.5	antiferromagnet, k = (0, 0, 0)	this study
$Ba_2MnGe_2O_7$	$P\bar{4}2_1m$	4.66	2D-AFM, k = (0, 0, 1/2)	9
$Ba_2CoGe_2O_7$	$P\bar{4}2_1m$	6.7	2D-AFM, k = (0, 0, 0), multiferroic behavior	10−14
$Ba_2CuGe_2O_7$	$P\bar{4}2_1m$	3.26	2D-spiral AFM, incommensurate−commensurate transition	15
$Ln_2GeBe_2O_7$	$P\bar{4}2_1m$		Ln = Y, La, Pr, Sm, Gd, Dy; paramagnet (T > 5 K)	16
$Eu_2MgSi_2O_7$	$P\bar{4}2_1m$		paramagnet (T > 1.8 K)	5
$Eu_2MnSi_2O_7$	$P\bar{4}2_1m$	10.7	ferrimagnet	5

source equipped with a curved graphite monochromator. The data were collected by step-scanning in the angle range of $10° \leq 2\theta \leq 120°$ at a step size of 0.02°. For $Sr_2MnGe_2O_7$ and $Sr_2CoGe_2O_7$, the neutron powder diffraction (NPD) measurements were collected in the range $3° \leq 2\theta \leq 152°$ using a 2θ step size of 0.1° with the wavelength of 1.84843 Å, at low temperature (2.5−20 K). The measurements were performed on the Kinken powder diffractometer for high-resolution measurements, HERMES, of the Institute for Materials Research (IMR), Tohoku University,[20] installed at the JRR-3 M Reactor in the Japan Atomic Energy Agency (JAEA), Tokai. The XRD and NPD data were analyzed by the Rietveld method using the program RIETAN-FP,[21] and the crystal and magnetic structures were drawn by using the VESTA program.[22]

2.3. Magnetic Measurements.

The temperature dependence of the magnetic susceptibilities were measured with a SQUID magnetometer (Quantum Design, MPMS-5S). The measurements were performed under both zero-field-cooled (ZFC) and field-cooled (FC) conditions over the temperature range between 1.8 and 300 K in an applied magnetic field of 0.1 T. The field dependence of the magnetizations was measured over the magnetic field range between −5 and 5 T at 5 K. The remnant magnetization measurements were also performed. The sample was cooled to 1.8 K in a zero magnetic field. The magnetic field was applied up to 5 T and then reduced to zero, and the magnetization measurements were preformed in the temperature range from 1.8 to 30 K

2.4. Specific Heat Measurements.

The specific heat measurements were performed using a relaxation technique with a commercial physical property measurement system (Quantum Design, PPMS) in the temperature range of 1.8−300 K. The pelletized sample was mounted on a thin alumina plate with Apiezon N-grease for better thermal contact.

3. RESULT AND DISCUSSION

3.1. Crystal Structure.

The melilite-type oxides $Sr_2MGe_2O_7$ (M = Mn, Co, Zn) were successfully prepared. They were obtained as white (M = Mn, Zn) or blue (Co) colored polycrystalline samples. Their X-ray diffraction (XRD) profiles are shown in Figure S1 (Supporting Information). The observed peaks were indexed on a tetragonal unit cell ($a \sim 8$ Å, $c \sim 5$ Å) with the space group $P\bar{4}2_1m$, which is typical for the melilite-type compounds.[2,3] Among these three compounds, only the $Sr_2MnGe_2O_7$ contains a small amount of α-Sr_2GeO_4 (~1%) as an impurity.[24] All XRD data were analyzed by the Rietveld method using the structural model for $Sr_2ZnGe_2O_7$.[23] The calculated profiles are plotted in Figure S1 (Supporting Information), and the refined structural parameters and reliability factors are summarized in Table S1 (Supporting Information). For Co and Zn compounds, the structural parameters are in good agreement with the results reported previously.[19,23] On the other hand, the lattice parameters of the Mn compound are different from those by earlier researchers.[19] This is due to the fact that the oxidation state of Mn ions is different between our sample and earlier researchers' sample (ref 19). In this study, we prepared $Sr_2MnGe_2O_7$ in an evacuated quartz tube. On the other hand, the earlier researchers prepared their sample in air. To clarify this point, we also prepared $Sr_2MnGe_2O_7$ in air. The lattice parameters prepared in air are in good agreement with those by earlier researchers, which is shown in Table S2 and Figure S2 in the Supporting Information.

The neutron powder diffraction (NPD) measurements for $Sr_2MnGe_2O_7$ and $Sr_2CoGe_2O_7$ (at 20, 2.5 K) were carried out to obtain further information about the structural and magnetic properties. The NPD profiles are shown in Figures 2 and 3. For the data collected at 20 K, all observed peaks were indexed with the structural model determined by the XRD measurement at room temperature. Thus, no structural phase transition occurs at low temperatures. We carried out the Rietveld analysis of these NPD data taking into account the possibilities of the cation disorder between M and M′ sites and the oxygen defect. However, no evidence of such possibilities has not been found. The structural parameters for Mn and Co compounds are shown in Tables 2 and 3, respectively. At 2.5 K, additional diffraction peaks are observed. As will be discussed later, they are due to an antiferromagnetic ordering of Mn^{2+} or Co^{2+} moments.

The schematic crystal structure of the title compounds is illustrated in Figure 1, and some selected interatomic distances calculated from the structural parameters are listed in Table 4. In this structure, both the M and the Ge ions occupy the

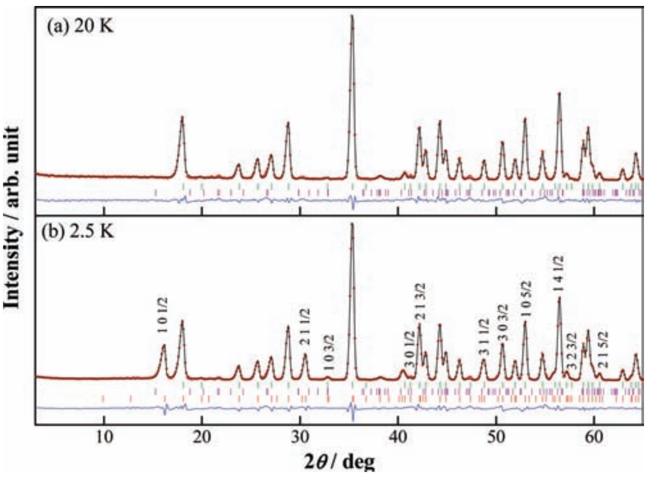

Figure 2. Powder neutron diffraction profiles for $Sr_2MnGe_2O_7$ at (a) 20 and (b) 2.5 K. The calculated and observed profiles are shown as the top black solid line and red markers, respectively. In (a), the vertical marks in the middle show positions calculated for Bragg reflections of $Sr_2MnGe_2O_7$. The second vertical markers show positions for an impurity of α-Sr_2GeO_4. In (b), the third vertical marks show the magnetic Bragg reflections for $Sr_2MnGe_2O_7$. The lower trace is a plot of the difference between calculated and observed intensities.

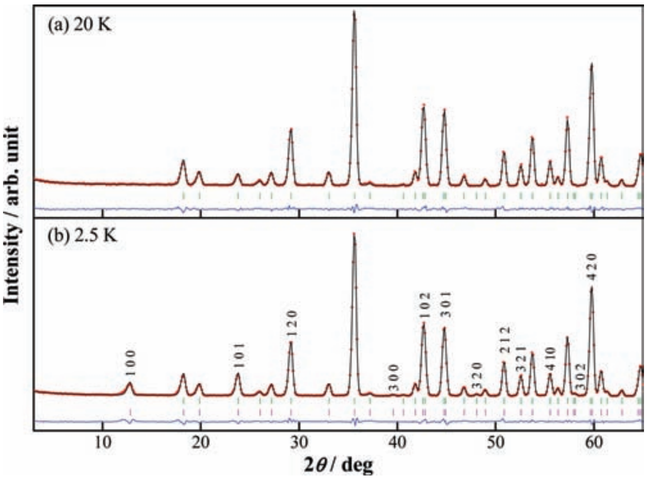

Figure 3. Powder neutron diffraction profiles for $Sr_2CoGe_2O_7$ at (a) 20 and (b) 2.5 K. The calculated and observed profiles are shown as the top black solid line and red cross markers, respectively. In (b), the second vertical marks show the magnetic Bragg reflections for $Sr_2CoGe_2O_7$. The lower trace is a plot of the difference between calculated and observed intensities.

tetrahedral sites, and the MO_4 and GeO_4 tetrahedra form a two-dimensional network by sharing corner-oxygen ions. On the other hand, the Sr ions are coordinated by eight oxygen ions and locate between networks. The bond valence sums (BVS)[25,26] are calculated from the interatomic distances, and they are also shown in Table 4. These values indicate that the Sr and M ions are in the divalent state and the Ge ion is in the tetravalent state. The magnetic ions (Mn^{2+} and Co^{2+}) occupy the M site. In this structure, the M−O−M superexchange pathway along the c axis does not exist. The possible magnetic pathway is the M−O−O−M one in the basal *ab* plane.

3.2.1. Magnetic Susceptibility.

$Sr_2MnGe_2O_7$. Figure 4 shows the temperature dependence of the magnetic susceptibility for $Sr_2MnGe_2O_7$. No deviation is found between the ZFC and the FC in the measured temperature range. The data were fitted by the Curie−Weiss law between 100 and 300 K, using the equation

$$\chi_M = \frac{C}{T - \theta} + \chi_{TIP} \quad (1)$$

where C, θ, and χ_{TIP} mean the Curie constant, Weiss constant, and temperature-independent paramagnetic susceptibility, respectively. The effective magnetic moment (μ_{eff}) was determined to be 5.84(2) μ_B/Mn, which is close to the spin-only value expected for the Mn^{2+} ($3d^5$) ion in a high-spin state (5.92 μ_B). The Weiss constant θ is −10.6(1) K, and the negative θ value indicates that the predominant magnetic interaction between Mn^{2+} ions is antiferromagnetic.

Table 2. Structural Parameters for $Sr_2MnGe_2O_7$ by NPD Data

atom	site	x	y	z	B (Å^2)
			20 K[a]		
Sr	4e	0.1659(2)	0.6660	0.50161(3)	0.22(5)
Mn	2a	0	0	0	0.15(9)
Ge	4e	0.6408(1)	0.1408	0.9427(4)	0.24(5)
O(1)	2c	0	1/2	0.1860(7)	0.24(5)
O(2)	4e	0.6387(2)	0.1387	0.2674(5)	0.34(6)
O(3)	8f	0.0800(2)	0.1842(2)	0.2167(4)	0.29(5)
			2.5 K[b]		
Sr	4e	0.1656(2)	0.6656	0.5062(4)	0.29(4)
Mn	2a	0	0	0	0.21(10)
Ge	4e	0.6405(2)	0.1405	0.9427(4)	0.35(4)
O(1)	2c	0	1/2	0.1862(7)	0.41(8)
O(2)	4e	0.6389(2)	0.1389	0.2674(4)	0.36(5)
O(3)	8f	0.0801(2)	0.1844(2)	0.2167(4)	0.37(4)

[a] Space group $P\bar{4}2_1m$ (No. 113), Z = 2, a = 8.2833(26) Å, c = 5.3096(16) Å, V = 364.31(19) Å^3, R_{wp} = 5.99%, R_p = 4.34%, R_B = 1.11%, R_F = 0.46%. [b] Space group $P\bar{4}2_1m$ (No. 113), Z = 2, a = 8.2838(1) Å, c = 5.3100(1) Å, V = 364.38(1) Å^3, μ_{Mn} = 3.99(5) μ_B, R_{wp} = 5.84%, R_p = 4.17%, R_B = 1.12%, R_F = 0.52%, $R_{mag\ B}$ = 2.13%, $R_{mag\ F}$ = 0.66%,

Table 3. Structural Parameters for $Sr_2CoGe_2O_7$

atom	site	x	y	z	B (Å^2)
			20 K[a]		
Sr	4e	0.1653(1)	0.6653	0.5065(3)	0.24(4)
Co	2a	0	0	0	0.20(11)
Ge	4e	0.6425(1)	0.1425	0.9496(2)	0.29(4)
O(1)	2c	0	1/2	0.1818(5)	0.27(6)
O(2)	4e	0.6384(2)	0.1384	0.2738(3)	0.37(5)
O(3)	8f	0.0818(2)	0.1792(2)	0.2094(3)	0.39(4)
			2.5 K[b]		
Sr	4e	0.1653(1)	0.6653	0.5069(2)	0.20(3)
Co	2a	0	0	0	0.12(9)
Ge	4e	0.6424(1)	0.1424	0.9494(2)	0.29(3)
O(1)	2c	0	1/2	0.1818(5)	0.29(6)
O(2)	4e	0.6384(2)	0.1384	0.2737(3)	0.39(4)
O(3)	8f	0.0816(2)	0.1793(2)	0.2095(3)	0.43(4)

[a] Space group $P\bar{4}2_1m$ (No. 113), Z = 2, a = 8.1616(25) Å, c = 5.3103(16) Å, V = 353.72(18) Å^3, R_{wp} = 4.64%, R_p = 3.50%, R_B = 0.84%, R_F = 0.35%. [b] Space group $P\bar{4}2_1m$ (No. 113), Z = 2, a = 8.1621(2) Å, c = 5.3101(1) Å, V = 353.76(1) Å^3, μ_{Mn} = 2.84(5) μ_B, R_{wp} = 4.15%, R_p = 3.03%, R_B = 0.75%, R_F = 0.31%, $R_{mag\ B}$ = 3.19%, $R_{mag\ F}$ = 0.45%

Table 4. Selected Interatomic Distances (Å) and Bond Valence Sums

	$Sr_2MnGe_2O_7$		$Sr_2CoGe_2O_7$		$Sr_2ZnGe_2O_7$
	XRD (RT)	NPD (20 K)	XRD (RT)	NPD (20 K)	XRD (RT)
Sr−O(3) × 2	2.561(6)	2.572(3)	2.558(4)	2.559(1)	2.568(6)
Sr−O(1)	2.571(8)	2.582(3)	2.568(5)	2.572(1)	2.576(5)
Sr−O(2)	2.589(5)	2.615(3)	2.589(5)	2.580(2)	2.589(6)
Sr−O(2)′ × 2	2.746(3)	2.805(2)	2.742(4)	2.748(2)	2.755(4)
Sr−O(3)′ × 2	2.903(6)	2.838(2)	2.904(1)	2.857(1)	2.875(5)
BVS (Sr^{2+})	1.72	1.73	1.78	1.82	1.77
M−O3 × 4	2.033(6)	2.023(2)	1.957(6)	1.954(1)	1.941(5)
BVS (M^{2+})	2.08	2.13	1.95	1.96	2.10
Ge−O2	1.714(6)	1.724(3)	1.715(7)	1.722(2)	1.708(5)
Ge−O3 × 2	1.717(6)	1.752(2)	1.726(6)	1.753(1)	1.742(5)
Ge−O1	1.798(4)	1.786(3)	1.796(5)	1.786(2)	1.786(4)
BVS (Ge^{4+})	4.15	3.94	4.10	3.94	4.042

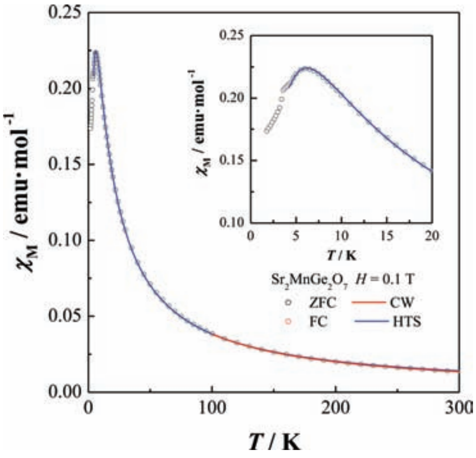

Figure 4. Temperature dependence of the magnetic susceptibility of $Sr_2MnGe_2O_7$. The red and blue solid lines are fitting results by the Curie−Weiss law (CW) and the high-temperature series (HTS) expansion for a square-planar lattice, respectively.

At low temperatures, the data show a maximum at 6.0 K and another anomaly at ∼4 K (see the inset of Figure 4). The former feature is often found in the low-dimensional magnet.[1,27] In this compound, the arrangement of the Mn^{2+} ions can be regarded as the square-planar lattice if the interlayer magnetic interaction is much weaker. The observed magnetic susceptibility (5−300 K) was fitted by using a high-temperature series (HTS) expansion of the square-planar lattice for the Heisenberg model

$$\chi_M = \frac{N_A g^2 \mu_B^2 S(S+1)}{3k_B T} \sum a_n (J/k_B T)^n \qquad (2)$$

where N_A, g, μ_B, k_B, and J are the Avogadro constant, g factor, Bohr magnetion, Bolzmann constant, and exchange integrals for the nearest-neighbor Mn−Mn ions in the ab plane, respectively, and a_n (n = 1−8) are the coefficients given in previous results.[28−31] The fitting equation was obtained by applying the Padé approximation ([4, 4] Padé) to eq 2. We calculated the g factor and J as fitting parameters. The calculation result is shown in Figure 4 as a solid blue line, and it is in good agreement with the experimental data. The g factor of the Mn^{2+} ion and the value of J are determined to be 1.92(1) and −0.34(1) K, respectively. The effective magnetic moment μ_{eff} and the Weiss constant θ were calculated to be 5.68 μ_B and −7.93K, respectively, from the equations $\mu_{eff} = gS(S+1)^{1/2}$ and $q = \sum 2zJS(S+1)/3k_B$, where z = 4. These values are comparable to those estimated from the Curie−Weiss law (5.92 μ_B and −10.6 K). This fitting indicates that $Sr_2MnGe_2O_7$ shows a two-dimensional behavior despite the shorter Mn−Mn distance along the c axis (interlayer, 5.32 Å) compared with that in the ab plane (intralayer, 5.86 Å). That is, it is a reasonable approximation to ignore the next-nearest-neighbor interaction. A comparable magnitude of the J value has been reported for the analogous compound $Ba_2MnGe_2O_7$ ($|J|$ = 0.323 K in the ab plane, $|J'|$ = 0.0012 K along the c axis) from the inelastic neutron scattering measurements.[9]

Figure 5a shows the temperature dependence of the specific heat for $Sr_2MnGe_2O_7$. The data show a λ-type anomaly at 4.4 K, indicating the occurrence of the long-range antiferromagnetic ordering of Mn^{2+} ions. The magnetic entropy (S_{mag}) due

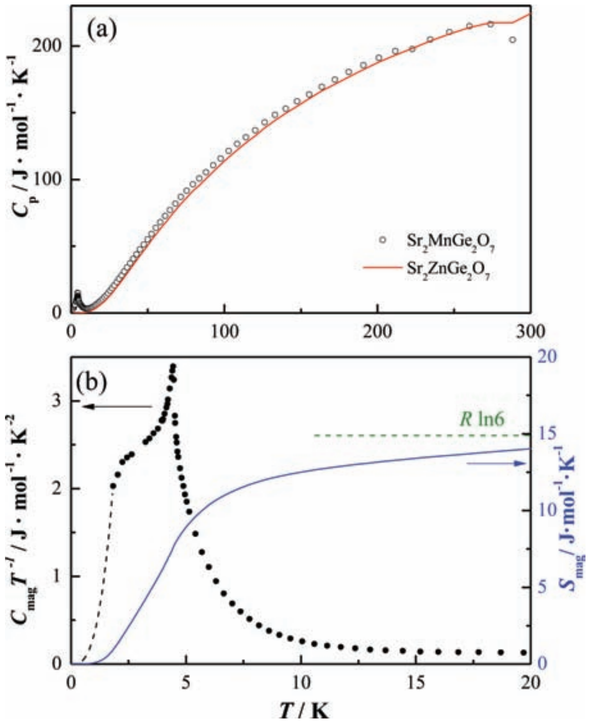

Figure 5. Temperature dependence of (a) specific heat (C_P), and (b) magnetic specific heat divided by temperature (C_{mag} T^{-1}) and magnetic entropy (S_{mag}) for $Sr_2MnGe_2O_7$.

to the magnetic ordering was calculated by using $S_{mag} = \int_0^T C_{mag}/T \, dT$, in which the magnetic specific heat (C_{mag}) was estimated by subtracting the lattice and electronic specific heat from the experimental specific heat of $Sr_2MnGe_2O_7$. For the lattice and electronic contributions, we used the specific heat of a nonmagnetic and isostructural compound $Sr_2ZnGe_2O_7$. The magnetic specific heat below 1.8 K was extrapolated by the relation $C_{mag} \propto T^3$ from the spin-wave model for an antiferromagnet.[32] The temperature dependence of the magnetic specific heat divided by temperature (C_{mag}/T) and magnetic entropy (S_{mag}) are plotted in Figure 5b. The S_{mag} value reaches 13.9 J mol^{-1} K^{-1} at 20 K, which is close to the theoretical value $R \ln(2S + 1) = R \ln 6 = 14.90$ J mol^{-1} K^{-1} (R = gas constant). This result shows that the observed magnetic transition is due to the long-range antiferromagnetic ordering of the Mn^{2+} ion in a high-spin configuration with $S = 5/2$.

Figure 2b is a powder neutron diffraction profile measured at 2.5 K. The data show a number of low-angle peaks, which are associated with the antiferromagnetic transition found from the magnetic susceptibility and specific heat measurements. All of theses reflections can be indexed using a propagation vector $\boldsymbol{k} = (0, 0, 1/2)$; that is, the magnetic unit cell is represented as $a_{mag} = a$, $c_{mag} = 2c$. To determine all the possible magnetic structures compatible with the crystal symmetry ($P\bar{4}2_1m$), the representational analysis was performed using the program SARAh.[33] For the Mn^{2+} ions on the 2a site, the decomposition of magnetic representation is

$$\Gamma = 1\Gamma_1^1 + 1\Gamma_2^1 + 0\Gamma_3^1 + 0\Gamma_4^1 + 2\Gamma_5^2 \qquad (3)$$

The constraint from the Landau theory requires three possible magnetic structures (the representations Γ_1, Γ_2, and Γ_5), and basis vectors for these representations are listed in Table 5. The Mn site is divided into two magnetic sublattices, Mn1 (0, 0, 0) and Mn2 (1/2, 1/2, 0). The Γ_1 and Γ_2 represent the collinear antiferromagnetic structures along the c axis, in which the Mn1 and Mn2 spins are antiparallel or parallel arrangements. On the other hand, the Γ_5 means noncollinear antiferromagnetic structures with orthogonal spin arrangements in the ab plane. The best fit was only achieved by using a model including the representation Γ_1. The calculated profiles are plotted in Figure 2, and the magnetic structure is illustrated in Figure 10a. The results of the Rietveld analysis are listed in Table 2. The ordered magnetic moment of the Mn^{2+} ion is determined to be 3.99(5) μ_B. The smaller value than the theoretical moment (5 μ_B) expected from the high-spin 3d^5 configuration is due to the fact that neutron diffraction measurements were performed just below T_N.

Table 5. Basis Function of the Irreducible Group Representation of the Space Group $P\bar{4}2_1m$ Appearing in the Magnetic Representation with $\boldsymbol{k}$ = (0, 0, 1/2)

		Mn(1)[a]			Mn(2)[a]		
irreducible group	basis vector	m_x	m_y	m_z	m_x	m_y	m_z
Γ_1	Ψ_1	0	0	4	0	0	−4
Γ_2	Ψ_2	0	0	4	0	0	4
Γ_5	Ψ_3	2	0	0	0	−2	0
	Ψ_4	0	2	0	−2	0	0
	Ψ_5	0	−2	0	−2	0	0
	Ψ_6	2	0	0	0	2	0

[a] The atoms of the nonprimitive basis are defined as (0, 0, 0) for Mn(1) and (1/2, 1/2, 0) for Mn(2) in $Sr_2MnGe_2O_7$.

In this magnetic structure, the magnetic interaction of Mn ions in the ab plane (next-nearest-neighbor) is antiferromagnetic and it is predominant, that is, thus the 2D nature in the temperature dependence of the magnetic susceptibility with the negative J value. In addition, the magnetic interaction of Mn ions along the c axis is also antiferromagnetic. $Sr_2MnGe_2O_7$ has the same magnetic structure as that of the $Ba_2MnGe_2O_7$. The difference between these two compounds is in the direction of ordered magnetic moment, parallel or perpendicular ($\parallel c$ or $\perp c$).[9]

3.2.2. $Sr_2CoGe_2O_7$. Figure 6 shows the temperature dependence of the reciprocal magnetic susceptibility for $Sr_2CoGe_2O_7$.

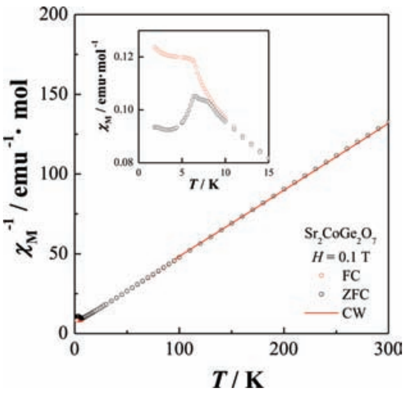

Figure 6. Temperature dependence of the reciprocal magnetic susceptibility of $Sr_2CoGe_2O_7$. The red solid line is a fitting result by the Curie−Weiss law (CW). The inset shows the susceptibility vs temperature curve at low temperatures.

From the result of fitting the data above 100 K by using eq 1, the effective magnetic moment was determined to be 4.43(5) μ_B/Co. This value is somewhat larger than the spin-only value (3.87 μ_B) of the 3d^7 ion in a tetrahedral coordination ($S = 3/2$), which may be due to the effect of orbital angular momentum.[34] A similar value (4.3 μ_B) has been observed for the analogous melilite $Ba_2CoSi_2O_7$ (4.3 μ_B).[7]The negative θ value (−18.1(6) K) indicates that the predominant magnetic interaction between Co^{2+} ions is antiferromagnetic.

The ZFC and FC magnetic susceptibilities for $Sr_2CoGe_2O_7$ in the low-temperature range are plotted in the inset of Figure 6. The data show two anomalies: the large divergence between ZFC and FC susceptibilities at 8.4 K and a cusp in the susceptibility versus temperature curve at 6.4 K, which indicates the existence of a small ferromagnetic moment. To study the ferromagnetic moment, the remnant magnetization measurements were performed. The field dependence of magnetization and the temperature dependence of the remnant magnetization are shown in Figures 7 and 8, respectively. The remnant magnetization rapidly decreases at 6.7 K. Both data show that the remnant magnetization is very small (~0.001 μ_B). This weak ferromagnetic component associated with the magnetic transition is due to the Dzyaloshinsky−Moriya interaction.[10,15]

Figure 9a shows the temperature dependence of the specific heat. A λ-type anomaly is observed at 6.5 K, indicating the occurrence of the long-range antiferromagnetic ordering of Co^{2+} ions. By the same way as the case for $Sr_2MnGe_2O_7$, the magnetic entropy is obtained and it reaches 10.6 J mol^{-1} K^{-1} at 20 K, which is close to the theoretical value for $S = 3/2$ ion, that

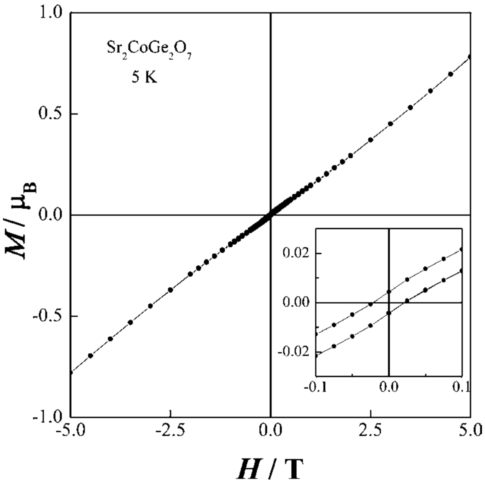

Figure 7. Field dependence of the magnetization for $Sr_2CoGe_2O_7$ at 5 K.

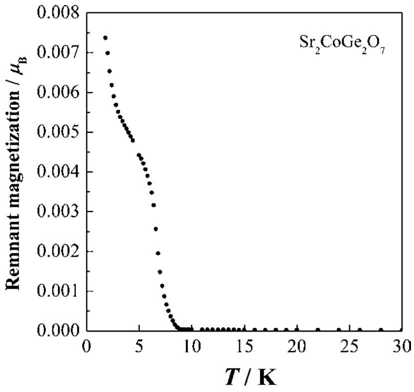

Figure 8. Temperature dependence of the remnant magnetization for $Sr_2CoGe_2O_7$.

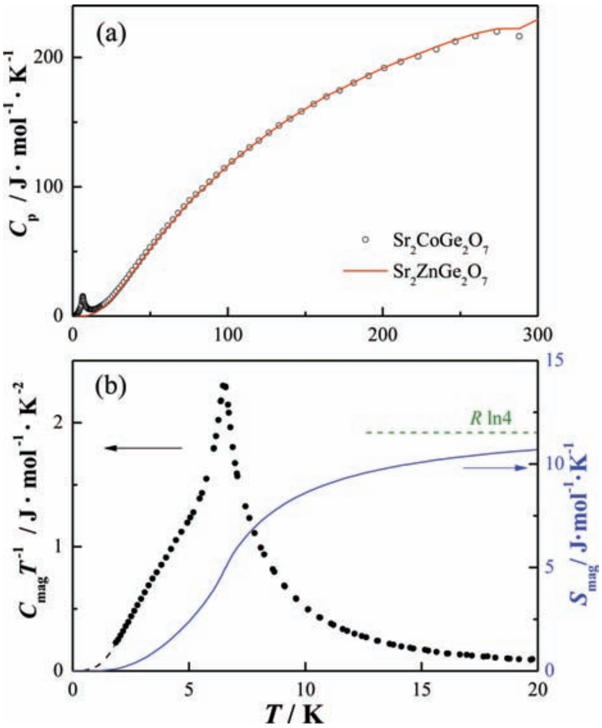

Figure 9. Temperature dependence of (a) specific heat (C_P), and (b) magnetic specific heat divided by temperature (C_{mag} T^{-1}) and magnetic entropy (S_{mag}) for $Sr_2CoGe_2O_7$.

Table 6. Basis Function of the Irreducible Group Representation of the Space Group $P\bar{4}2_1m$ Appearing in the Magnetic Representation with k = (0, 0, 0)

		Co(1)[a]			Co(2)[a]		
irreducible group	basis vector	m_x	m_y	m_z	m_x	m_y	m_z
Γ_1	Ψ_1	0	0	4	0	0	−4
Γ_2	Ψ_2	0	0	4	0	0	4
Γ_5	Ψ_3	4	0	0	0	0	0
	Ψ_4	0	0	0	0	−4	0
	Ψ_5	0	0	0	−4	0	0
	Ψ_6	0	−4	0	0	0	0

[a] The atoms of the nonprimitive basis are defined as (0, 0, 0) for Co(1) and (1/2, 1/2, 0) for Co(2) in $Sr_2CoGe_2O_7$.

is, $R \ln(2S + 1) = R \ln 4 = 11.52$ J mol^{-1} K^{-1}. This result shows that the observed magnetic transition is due to the antiferromagnetic ordering of the Co^{2+} ion.

The neutron diffraction measurements were carried out at low temperatures (2.5 and 20 K). The data at 2.5 K show the magnetic Bragg reflections at lower angles. These reflections can be indexed using a propagation vector $\boldsymbol{k}$ = (0, 0, 0); that is, the magnetic cell is the same as the crystal one. From the representational analysis, the decomposition of magnetic representation is obtained

$$\Gamma = 1\Gamma_1^1 + 1\Gamma_2^1 + 0\Gamma_3^1 + 0\Gamma_4^1 + 2\Gamma_5^2 \qquad (4)$$

The basis vectors for each irreducible representation are shown in Table 6. The representations Γ_1 and Γ_2 represent the collinear antiferromagnetic and ferromagnetic structures along the c axis, respectively. From the representation Γ_5, various magnetic structures can be led, in which all the magnetic moments lay on the ab plane. We tried to explain the diffraction data by these models; finally, we have succeeded in determining the magnetic structure as the linear combination of basis vectors belonging to Γ_5. The calculated profiles are plotted in Figure 3, the magnetic structure is illustrated in Figure 10b, and the results of the Rietveld analysis are shown in Table 3. In this magnetic structure, the magnetic moments of Co1 (0, 0, 0) and Co2 (1/2, 1/2, 0) sublattices adopt a parallel arrangement. The ordered magnetic moment for the Co^{2+} ion is determined to be 2.81(5) μ_B at 2.5 K, which is in good agreement with the 3 μ_B expected from the 3d ^{7} ion. The magnetic moments of the Co^{2+} ion lie in the ab plane, but its exact directions could not be determined because the magnetic structure of $Sr_2CoGe_2O_7$ has a tetragonal symmetry, as shown

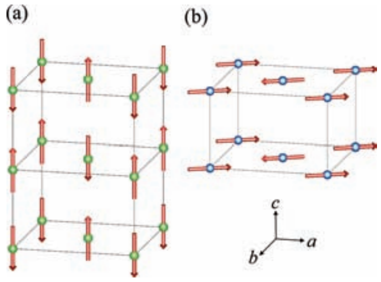

Figure 10. Magnetic structure of (a) $Sr_2MnGe_2O_7$ and (b) $Sr_2CoGe_2O_7$. Diamagnetic ions are omitted.

in Figure 10b. The magnetic moments of Mn^{2+} ions in the $Sr_2MnGe_2O_7$ are aligned along the *c* axis, while the Co^{2+} moments are confined in the *ab* plane of the $Sr_2CoGe_2O_7$. This result is mainly due to the anisotropic character of the Co^{2+} ions compared with the isotropic Mn^{2+}.

4. CONCLUSION

We investigated the synthesis, crystal structure, and magnetic properties of $Sr_2MGe_2O_7$ (M = Mn, Co). They crystallize in a tetragonal melilite-type structure with space group $P\bar{4}2_1m$. The magnetic susceptibility and specific heat measurements for $Sr_2MnGe_2O_7$ and $Sr_2CoGe_2O_7$ showed that an antiferromagnetic transition is observed at 4.4 and 6.5 K, respectively. Furthermore, the 2D-Heisenberg square lattice antiferromagnetic model can account for the magnetic susceptibility of $Sr_2MnGe_2O_7$. The magnetic structures for both compounds have been determined by neutron diffraction measurements.

In $Sr_2MnGe_2O_7$, the magnetic moment of Mn^{2+} is along the *c* axis. On the other hand, the magnetic moment of Co^{2+} in $Sr_2CoGe_2O_7$ is on the *ab* plane.

■ ASSOCIATED CONTENT

Ⓢ Supporting Information

Tables containing structural parameters, figures of powder X-ray diffraction profiles, and crystallographic data in CIF format. This material is available free of charge via the Internet at http://pubs.acs.org.

■ AUTHOR INFORMATION

Corresponding Author

*E-mail: t-endo38232@mail.sci.hokudai.ac.jp.

Notes

The authors declare no competing financial interest.

■ ACKNOWLEDGMENTS

This research was partially supported by the Global COE Program (Project No. B01: Catalysis as the Basis for Innovation in Materials Science) and a Grant-in-Aid for Young Scientists (No. 23750052) from Ministry of Education, Culture, Sports, Science and Technology.

■ REFERENCES

(1) De Joungh, L. J., Ed. *Kluwer Magnetic Properties of Layered Transition Metal Compounds*; Academic Publishers: Dordrecht, 1990; p 1.

(2) Burzo, E. Melilites and Related Silicates. *Landolt-Börnstein*; New Series; Springer: Berlin, 2005; Vol. *3/27*, p i2.

(3) Kaninskii, A. A.; Bohaty, L.; Becker, P.; Liebertz, J.; Held, P.; Eichler, H. J.; Rhee, H.; Hanuza, J. *Laser Phys. Lett.* **2008**, *5*, 845−868.

(4) Mill, B. V.; Baibakova, G. D. *Russ. J. Inorg. Chem.* **1990**, *35*, 341−343.

(5) Endo, T.; Doi, Y.; Wakeshima, M.; Hinatsu, Y. *Inorg. Chem.* **2010**, *23*, 10809.

(6) Akaki, M.; Tozawa, J.; Akahoshi, D.; Kuwahara, H. *J. Phys.: Conf. Ser.* **2009**, *150*, 042001.

(7) Adams, R. D.; Ralph, L.; Payen, C.; Datta, T. *Inorg. Chem.* **1996**, *35*, 3492−3497.

(8) Kenzelmann, M.; Zheludev, A.; Raymond, S.; Ressouche, E.; Masuda, T.; Böni, P.; Kakurai, K.; Tsukada, I.; Uchinokura, K.; Coldea, R. *Phys. Rev. B* **2001**, *64*, 054422.

(9) Masuda, T.; Kitaoka, S.; Takamizawa, S.; Metoki, N.; Kaneko, K.; Rule, K. C.; Kiefer, K.; Manaka, H.; Nojiri, H. *Phys. Rev. B* **2010**, *81*, 100402.

(10) Zheludev, A.; Sato, T.; Masuda, T.; Uchinokura, K.; Shirane, G.; Roessli, B. *Phys. Rev. B* **2003**, *68*, 024428.

(11) Sato, T.; Masuda, T.; Uchinokura, K. *Physica B* **2003**, *329−333*, 880−881.

(12) Yi, H. T.; Choi, Y. J.; Lee, S.; Cheong, S.-W. *Appl. Phys. Lett.* **2008**, *92*, 212904.

(13) Murakawa, H.; Onose, Y.; Miyahara, S.; Furukawa, N.; Tokura, Y. *Phys. Rev. Lett.* **2010**, *105*, 137202.

(14) Kézsmáki, I.; Kida, N.; Murakawa, H.; Bordács, S.; Onose, Y.; Tokura, Y. *Phys. Rev. Lett.* **2011**, *106*, 057403.

(15) Zheludev, A.; Maslov, S.; Shirane, G.; Sasago, Y.; Koide, N.; Uchinokura, K.; Tennant, D. A.; Nagler, S. E. *Phys. Rev. B* **1997**, *56*, 14006.

(16) Ochi, Y.; Morikawa, H.; Marumo, F.; Nozaki, H. *Yogyo Kyokaishi* **1983**, *91*, 229−234.

(17) Petrakovskii, G. A.; Bezmaternykh, L. N.; Gudim, I. A.; Sheptyakov, D.; Bayukov, O. A.; Vorotynov, A. M.; Velikanov, D. A.; Bovina, A. F. *Phys. Solid State* **2005**, *47*, 2114.

(18) Petrakovskii, G. A.; Bezmaternykh, L. N.; Gudim, I. A.; Bayukov, O. A.; Vorotynov, A. M.; Bovina, A. F.; Szymczak, R.; Baran, M.; Ritter, C. *Phys. Solid State* **2006**, *48*, **1906**.

(19) (a) Naruse, H.; Tanaka, K.; Morikawa, H.; Marumo, F. *Rep. Res. Lab. Eng. Mater., Tokyo Inst. Technol.* **1984**, *9*, 1−9; *Powder Diffr.* **1986**, *1*, 64−77.

(20) Ohoyama, K.; Kanouchi, T.; Nemoto, K.; Ohashi, M.; Kajitani, T.; Yamaguchi, Y. *Jpn. J. Appl. Phys.* **1998**, *37*, 3319−3326.

(21) Izumi, F.; Momma, K. *Solid State Phenom.* **2007**, *130*, 15−20.

(22) Momma, K.; Izumi, F. *J. Appl. Crystallogr.* **2008**, *41*, 653−658.

(23) Ochi, Y.; Tanaka, K.; Morikawa, H.; Marumo, F. *J. Mineral. Soc. Jpn.* **1982**, *15*, 331−341.

(24) Nishi, F.; Takeuchi, Y. *European Crystallographic Meeting* **1991**, *13*, 197.

(25) Brown, I. D.; Altermatt, D. *Acta Crystallogr., Sect. B* **1985**, *B41*, 244−247.

(26) Brese, N. E.; O'Keeffe, M. *Acta Crystallogr., Sect. B* **1991**, *B47*, 192−197.

(27) Carlin, R. L. *Magnetochemistry*; Springer-Verlang: Berlin, 1986; p 163.

(28) Rushbrooke, G. S.; Wood, P. J. *Proc. Phys. Soc., London* **1995**, *68*, 1161−9.

(29) Rushbrooke, G. S.; Wood, P. J. *Mol. Phys.* **1958**, *1*, 257−83.

(30) Stephenson, R. L.; Prinie, K.; Wood, P. J.; Eve, J. *Phys. Lett. A.* **1968**, *27*, 2−3.

(31) Yamaji, K.; Kondo, J. *J. Phys. Soc. Jpn.* **1973**, *35*, 25−32.

(32) Joshua, S. J.; Cracknell, A. P. *Phys. Rev. Lett.* **1969**, *A28*, 562−563.

(33) Wills, A. S. *Physica B* **2000**, *276−278*, 680−681.

(34) Carlin, R.L. *Transition Metal Chemistry*; Marcel Dekker, Inc.: New York, 1965; p 19.

■ NOTE ADDED AFTER ASAP PUBLICATION

This paper was published on the Web on February 29, 2012. Additional information was added to the Abstract, and the corrected version was reposted on March 1, 2012.